CHAPTER-3

Synthesis and characterizations of zinc ferrite particles and performance for OER

3.1. Abstract

The present research work describes the fabrication of zinc ferrite nanoparticles with varying stoichiometric compositions ($Zn_xFe_{3-x}O_4$; x= 0.25, 0.5, 0.75, and 1) and their electrocatalytic performance for OER. Egg white was employed as a precursor material during the thermal decomposition process to produce the catalysts. OER performances of four synthesized catalysts were investigated by physicochemical (XRD, FTIR and SEM) and electrochemical (CV, EIS, Tafel polarization) processes. Among four Zn ferrite catalysts of different stoichiometry, just $Zn_{0.25}Fe_{2.75}O_4$ exhibited the optimum catalytic activity, with the current density of 1 mA cm^{-2} at the overpotential of 454 mV, and with Tafel slope of 107 mV dec^{-1}. The Arrhenius plot was applied to determine thermodynamic parameters such as activation energy and electrochemical entropy of reaction, which were found to be 54.22 kJ mol^{-1} and -74 J K^{-1} mol^{-1}, respectively.

3.2. Introduction

Due to the wide range of use going from basic research to commercial usage in the field of medicine, magnetic storage, chemical industries [1], and biomedical applications including drug delivery, tissue repair, cell and tissue targeting and transfection, hyperthermia [2], magnetic oxide nanoparticles are now generating a lot of attention. Because of their electronic, optical, electrical, magnetic, and catalytic capabilities, spinel ferrite nanoparticles are recognized as one of the most significant inorganic nanomaterials. The structure of spinel ferrite is AFe_2O_4, where A and B represent the tetrahedral and octahedral cation sites, respectively, and O denotes the oxygen anion site [3]. Metal spinel ferrite nanoparticles have a

face-centered-cubic (fcc) compact packing structure and the general molecular formula MFe_2O_4 (*e.g.*, M=Zn, Ni, Co, Mn, or Mg). Zinc ferrite ($ZnFe_2O_4$) has gained the most attention among the spinel ferrite compounds because of its excellent chemical stability, robust electromagnetic performance, mechanical toughness, low coercivity, and mild saturation magnetization [4–6].

The main emphasis of the associated research and development operations is now put on the various processes for producing zinc ferrite nanoparticles. Numerous production processes, such as the ball-milling, sol-gel, co-precipitation [7], the aerogel process [3], the hydrothermal method [8], the reverse micelles process [9], and the micro-emulsion method [10] have been described to produce spinel zinc ferrite. Different precipitation agents, such as metal hydroxide in the co-precipitation process, surfactant and ammonia in the reverse micelles process, different micro-emulsion processes, and organic matrices in the sol-gel, have all been utilized to create specified size to form zinc ferrite nanoparticles. The majority of these processes have produced particles with necessary sizes and shapes, but because of their costly and complex processes, high reaction temperatures, lengthy reaction times, toxic reagents and by-products, and potential environmental harm, they are challenging to use on a large scale.

It becomes clear that employing egg white as a precursor provides a special and beneficial way when synthesizing Zn ferrite nanoparticles is contrasted with other approaches. Research has shown that egg white is a good complexing agent for material synthesis because of its water solubility and its capacity to bind metal ions. This allows for the successful synthesis of nano-crystalline Zn ferrites [11,12]. This process is notable for being effective, easy to prepare, and low cost. The desired structural and magnetic characteristics that the

produced nanoparticles displayed, underscoring the promise of egg white as a precursor in the production of functional materials [13]. When compared to alternative synthesis processes, egg white offers a viable path toward the economical and sustainable synthesis of Zn ferrite nanoparticles with customized characteristics [14,15]. Many literatures have been reported the synthesis of Zn ferrite via different synthesis routes, with electrocatalytic OER, summarized in **Table 3.1**.

Numerous proteins found in egg white, including globulin, ovomucin, and ovalbumin that have great nutritional value, strong gelling, foaming and emulsifying properties, and are soluble in water and readily amalgamate with metals. The ability of egg white proteins to foam aids in the creation of ferrites nanoparticles [16]. Egg white has been utilized as a binder combining gel for materials, especially bulk and porous ceramics, because of its solubility in water and capacity to combine with metal ions in solution [17]. The use of egg white contributes, and the procedure offers a different method as an option for the quick and affordable production of Zn ferrites [18].

Table 3.1. Comparison of various parameters of electrocatalytic OER for Zn ferrite-based materials reported in the literature.

Material	Synthesis technique	Support electrode	Overpotential (mV) / 10 mA cm^{-2}	Tafel slope / mV dec^{-1}	Electrolyte	References
$ZnFe_2O_4$	RF sputtering	ITO	497	91	1 M KOH	[19]
$ZnFe_2O_4$	-	NF	323	143	1 M KOH	[20]
$Co_{1-x}Zn_xFe_2O_4$	Pyrolysis	NF	317	79	1 M KOH	[21]
$ZnFe_2O_4$	Pyrolysis	NF	343	43	1 M KOH	[21]
$Zn_xCo_{3-x}O_4$	Hydrothermal	Ti Foil	320	51	1 M KOH	[22]
$ZnCo_2O_4$	Hydrothermal	NF	340	183	1 M KOH	[23]
Co–Zn/PNC	Pyrolysis	GCE	348	112	1 M KOH	[24]
$ZnFe_2O_4$	Solvothermal	NF	280	70	1 M KOH	[25]
$ZnFe_2O_4$/NG	Solvothermal	NF	240	63.5	1 M KOH	[26]
$ZnCo_2O_4$/rGO	Solvothermal	GCE	300	59.2	1 M KOH	[27]

$ZnFe_2O_4$	Spray pyrolysis	NF	319	115	1 M KOH	[28]
$ZnFe_2O_4$/ $ZnFe_2S_4$	Hydrothermal	NF	222	73.2	1 M KOH	[29]
$Zn_xFe_{3-x}O_4$	Thermal decomposition	GCE	454	107	1 M KOH	This work

Alternative energy sources are not a novel idea for humans, but in the twenty-first century, energy has emerged as the world's top worry. Fossil fuel reserves are finite, and by the middle of this century, they would be depleted [30]. The hunt for alternative and clean energy sources has quickened, especially as efforts are made to limit CO_2 emissions to lessen the effects of global warming. As an alternative, processes like photocatalytic water splitting have also been suggested as a potential method for creating pure hydrogen using solar energy [31,32]. This discussion has led to the discovery that producing hydrogen will be an essential part of our future energy systems [33], because the hydrogen and oxygen generated by water oxidation have no adverse effects on the environment [34]. It is challenging to produce minimal electrical energy consumption in the electrolytic cell, which is necessary for effective water electrocatalysis [35]. In order to do this, the right electrocatalysts must be used, and the hunt for materials that can lower overpotential value of both anodic and cathodic reactions has been increased [36].

Hydrogen energy is produced by the electrochemical water splitting. RuO_x and IrO_x, two metal oxide-based electrocatalysts used in this approach, exhibit strong OER activity

[37], even if they are less economical. Perovskites as electrocatalysts, also demonstrate the encouraging catalytic activity [38–40]. Therefore, the creation of an accessible, affordable metal-oxide based electrocatalyst is necessary.

Considering many electrocatalytic uses of synthetic zinc ferrite-based materials, the present work describes the use of Zn ferrite as an electrocatalyst in water splitting electrocatalysis. This material performs better when compared to other synthetic zinc ferrite-based material classes, other spinels, and perovskite oxides.

3.3. Experimental

3.3.1. Materials

Egg white, zinc nitrate hexahydrate ($Zn(NO_3)_2.6H_2O$) (AR, Sigma Aldrich, 99.9%), ferrous sulphate ($FeSO_4$) (AR, Merck, 99.9%).

3.3.2. Synthesis of zinc ferrite

$Zn_xFe_{3-x}O_4$ (x = 0.25, 0.5, 0.75, and 1.0); nano-sized zinc ferrites were produced via thermal decomposition method utilizing egg white as a precursor [27]. In 20 mL of double-distilled water, the stoichiometric ratios of pure zinc nitrate hexahydrate ($Zn(NO_3)_2{\cdot}6H_2O$) and ferrous sulphate ($FeSO_4$) as metal precursors were dissolved **(Table 3.2)**.

Table 3.2. Required stoichiometric amounts of metal precursors used for the synthesis of zinc ferrite nanoparticles.

Catalysts	**$Zn(NO_3)_2.6H_2O$**		**$FeSO_4$**	
	No. of moles	**Amount (g)**	**No. of moles**	**Amount (g)**
$Zn_{0.25}Fe_{2.75}O_4$	0.008	1.655	0.109	16.6748
$Zn_{0.5}Fe_{2.5}O_4$	0.017	3.2583	0.098	15.006
$Zn_{0.75}Fe_{2.25}O_4$	0.025	4.917	0.088	13.505
$ZnFe_2O_4$	0.034	6.556	0.079	12.004

The metal salts solution was then added dropwise into the egg white solution while vigorous stirring. The solution (30 mL) of egg white was agitated at room temperature until the solution turned milky white. At 100 ^oC, the resulting gel precursors were broken down and evaporated to create the light solid powder. The fluffy powder was thermally decomposed into the required oxide nanoparticles over the course of five hours in an electrical muffle furnace at 550 ^oC **(Figure 3.1)**.

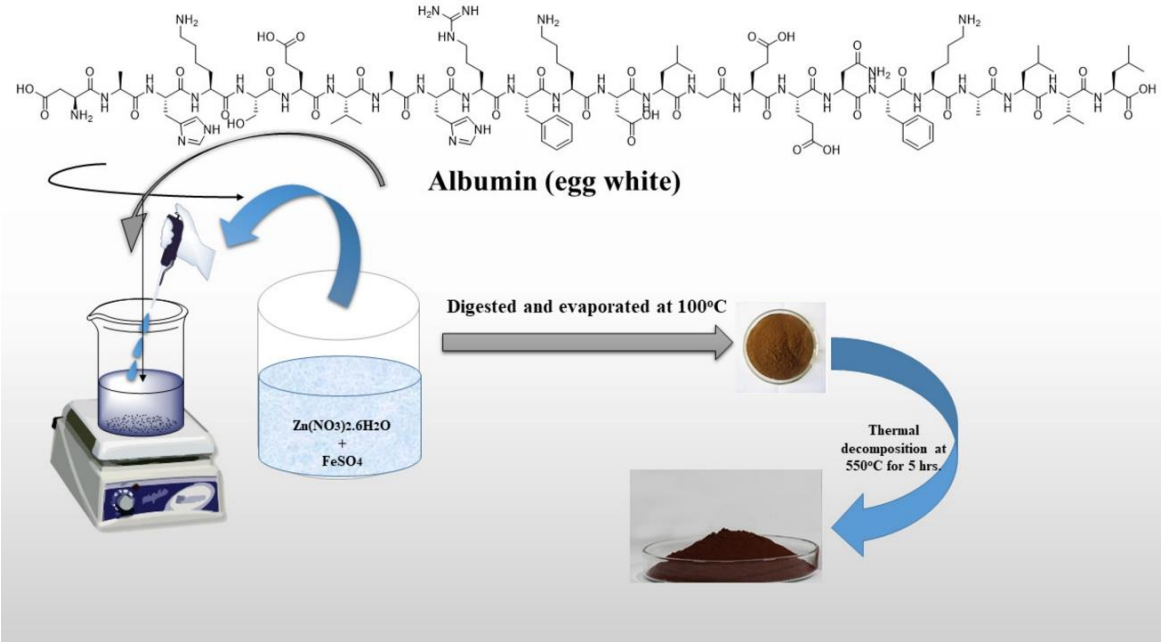

Figure 3.1. Schematic representation showing the thermal decomposition process used to create zinc ferrite nanoparticles from egg white.

3.3.3. Preparation of working electrode

An electrode made of glassy carbon served as support for the working electrode catalyst ink. To make the catalyst ink, 1 mg of the prepared catalyst (zinc ferrite nanoparticles) was dissolved in a solution of 20 µL Nafion (5%) and 40 µL ethyl alcohol, and then ultrasonicated for about an hour. The total resulting oxide ink (60 µL) was then dropwise-casted with the smallest droplet each followed by drying at room temperature. Before the drop casting, the GCE surface was cleaned and polished using alumina powder of sizes 1, 0.3, and 0.05 µm, respectively, for about 15 to 20 minutes. The prepared electrodes were then dried at room temperature.

3.3.4. Electrode preparation for spectro-electrochemical study

The obtained ink from the aforementioned method is used to prepare the working electrode for the *operando* spectro-electrochemical study. By immersing the platinum grid in the catalyst ink and then drying it at room temperature, the platinum grid is made ready to be used as a working electrode.

3.4. Characterizations

3.4.1. Physicochemical characterizations

In order to examine the structure of the $ZnFe_2O_4$ nanoparticles, diffraction patterns were made from powder crystalline samples at room temperature in the diffraction angle range of 5° to 80° using Shimadzu XRD 6000 diffractometer. FT-IR spectra were recorded in the range of 400 – 4000 cm^{-1} using a PerkinElmer model 1650 FT-IR spectrometer. The morphology of oxide powder was further studied by scanning electron microscope using Nova Nano-SEM 450 [FE-SEM] at different magnifications.

3.4.2. Electrochemical characterizations

A three-electrode, single compartment pyrex glass cell with 8 cm^2 area of Pt foil (Aldrich 99.9% pure) as a counter electrode, a working electrode of GC/oxide with a 0.07 cm^2 area, and a reference electrode of Hg/HgO/1M KOH, was used for all electrochemical studies. The Luggin capillary salt bridge was prepared using agar-agar and KCl. It connected the cell electrolyte to the reference electrode. All potentials provided in this study apply to the Hg/HgO/1M KOH reference electrode, having standard potential ($E^0_{Hg/HgO}$) equal to 105.3 mV

vs. NHE [41]. Using CHI-608C (CH instrument, USA), all electrochemical characterizations were performed using the same approaches as described above. These include cyclic voltammetry, impedance measurements, and Tafel polarization investigations [42–44].

According to the following **Equation 3.1**, all potential values measured by the Hg/HgO reference were converted to the reversible hydrogen electrode (RHE):

$$E_{RHE} = E_{Hg/HgO} + 0.0592 \times pH + E^{0}_{Hg/HgO} \quad \textbf{(3.1)}$$

3.4.3. Spectro-electrochemical characterizations

During spectro-electrochemical studies in a quartz cuvette, the catalyst ink immersed platinum grid served as the working electrode, platinum wire served as the counter electrode, and Hg/HgO in 1M KOH served as the reference electrode. The Luggin capillary salt bridge, which connected the reference electrode to the cell electrolyte, was built using agar-agar and KCl. During cyclic voltammetry, the spectra were captured at 20 mV s^{-1} scan rate closest to the onset potential. The *operando* spectro-electrochemical studies were carried out on ocean optics, FLAME-T-XR1-ES Assembly, 200 nm to 1025 nm range.

3.5. Results and discussion

3.5.1. Structural and morphological analysis

3.5.1.1. FT-IR study

The produced zinc substituted ferrite functional groups are visible in the FT-IR spectra in the 400 – 4000 cm^{-1} wave number range. **Figure 3.2** shows the recorded FT-IR spectra and displayed the typical absorption peaks at 430 cm^{-1} and 570 cm^{-1}, which are attributed to Fe-O

stretching vibrations in octahedral and tetrahedral voids, respectively. Position of bands corresponding to 430 cm^{-1} and 570 cm^{-1} are related to the bond lengths and their different position in the spectra is due to the different bond lengths of Fe^{3+}–O^{2-} at A and B sites [45]. Thus appearance of peak corresponding to higher frequency is attributed to the shorter bond-length of tetrahedral cluster and peak corresponding to lower frequency is attributed to longer bond length of octahedral cluster [46]. Another absorption band at 1110 cm^{-1} is attributed to a tetrahedral Fe^{3+}-O^{2-} stretching vibration. The stretching vibration of the C=C atom on the surface of the $ZnFe_2O_4$ nanoparticles was responsible for the extremely tiny band seen nearly 1580 cm^{-1} and the symmetric and asymmetric stretching causes the splitting around the band [47,48]. The band around 3000 cm^{-1} are due to the absorbed moisture from the atmosphere [49]. Water molecules were found on the surface of $ZnFe_2O_4$ nanoparticles as shown by the wide band absorption peak at 3590 cm^{-1} (bending mode of H_2O). The observed splitting in the bands at 3500 cm^{-1} in this spectra is due to the effect of terminated –OH on the tetrahedral, octahedral and bridging –OHs [49].

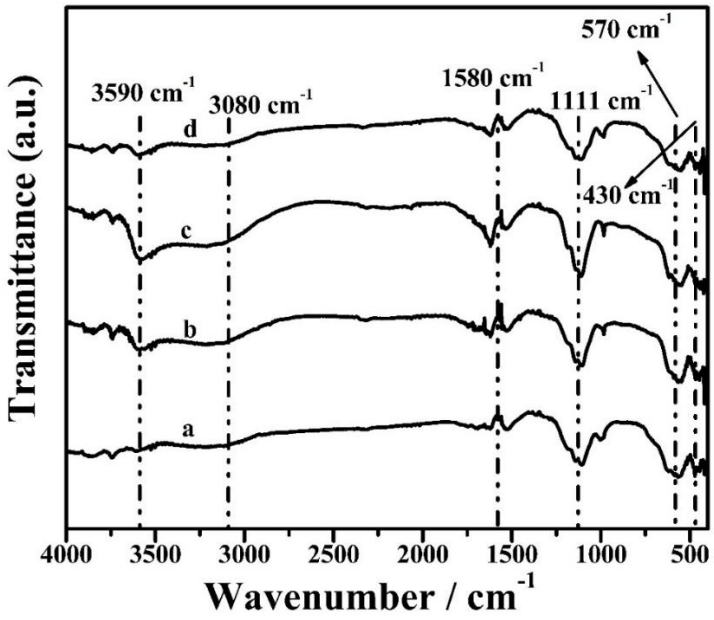

Figure 3.2. FT-IR spectra for $Zn_xFe_{3-x}O_4$ (x = 0.25, 0.5, 0.75 and 1.0) nanoparticles synthesized at 550 ^oC: **a)** $Zn_{0.25}Fe_{2.75}O_4$, **b)** $Zn_{0.5}Fe_{2.5}O_4$, **c)** $Zn_{0.75}Fe_{2.25}O_4$, **d)** $ZnFe_2O_4$.

3.5.1.2. XRD study

According to the JCPDS file No. 89-1009 for $ZnFe_2O_4$, the characteristic diffraction peaks for the spinel phase appear at specific 2θ angles, corresponding to the crystallographic planes (220), (311), (222), (400), (422), (511), and (440) of the spinel structure [50].These planes are indicative of the cubic spinel crystal structure of $ZnFe_2O_4$. The XRD powder patterns of the synthesized samples, as illustrated in **Figure 3.3**, exhibit prominent peaks that align with these planes, confirming the development of the spinel phase in the zinc-substituted oxides. In addition to the spinel phase peaks, the XRD patterns also reveal the presence of additional peaks that do not conform to the $ZnFe_2O_4$ spinel structure. These extraneous peaks suggest the presence of secondary phases, identified as α-Fe_2O_3 (hematite) and ZnO (zincite), which are

common impurities in the synthesized samples [51,52]. This iron oxide phase is a common by-product in the synthesis of ferrites and is characterized by its distinct diffraction peaks. The phase corresponds to zinc oxide also exhibits unique diffraction peaks distinguishable from the spinel structure. The occurrence of these impurity phases, despite the high-temperature synthesis, can be attributed to incomplete reaction or segregation of precursor materials during the calcination process. Their presence in all calcined samples suggests a systematic issue related to the synthesis conditions or the inherent stability of these phases under the given conditions [53].

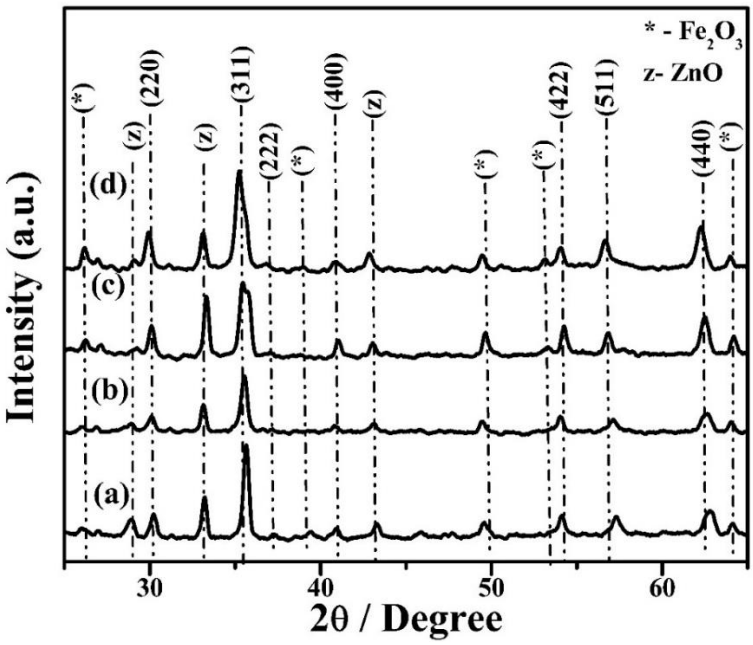

Figure 3.3. XRD patterns of zinc ferrite nanoparticles prepared at 550 ^{o}C: **a)** $Zn_{0.25}Fe_{2.75}O_4$, **b)** $Zn_{0.5}Fe_{2.5}O_4$, **c)** $Zn_{0.75}Fe_{2.25}O_4$, **d)** $ZnFe_2O_4$.

3.5.1.3. SEM study

The FE-SEM micrographs in **Figure 3.4 (a–d)** depict $ZnFe_2O_4$ and $Zn_{0.25}Fe_{2.75}O_4$ samples. These images illustrate that most particles adopt a nearly square clustered shape and are unevenly distributed throughout the samples. From the obtained results, it was clear that the synthesized particles were slightly agglomerated with grain boundaries due to their ferrimagnetic nature [54–56]. However, the particle sizes are noticeably non-uniform. To determine the average particle size, the particle size distribution histograms were analyzed and fitted to a log-normal distribution function **(Equation 3.2)** [57].

$$f(D) = \left(\frac{1}{\sqrt{2\pi}\sigma_D}\right) \exp\left[-\frac{\ln^2\left(\frac{D}{D_0}\right)}{2\sigma^2}\right] \qquad \textbf{(3.2)}$$

Where D corresponds to average particle size and σ is the standard deviation. Typical fitting of log normal distribution function to particle size distribution histogram for $Zn_{0.25}Fe_{2.75}O_4$ sample is illustrated in **Figure 3.4 (e).**

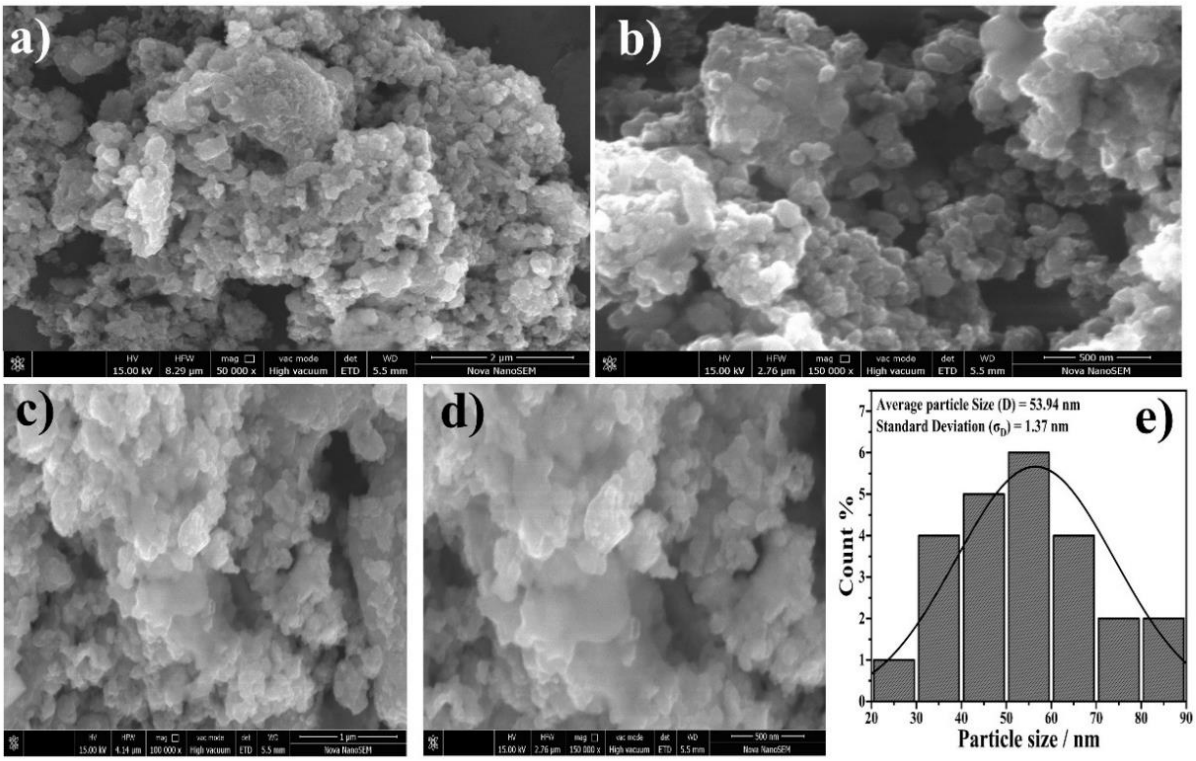

Figure 3.4. SEM micrographs; **a, b)** $ZnFe_2O_4$ at different magnifications, **c, d)** $Zn_{0.25}Fe_{2.75}O_4$ at different magnifications, **e)** particle size distribution of $ZnFe_2O_4$ fitted with log normal distribution function.

3.5.2. Electrochemical analysis

Inks of catalysts deposited on glassy carbon (GCE) conductive substrates, *i.e.,* zinc ferrites, $Zn_xFe_{3-x}O_4$ (x = 0.25, 0.5, 0.75, 1) were examined for their electrocatalytic activity. To detect the occurrence of redox reaction on the oxide/electrolyte interface, the cyclic voltammogram of each oxide on a GCE support was recorded in the potential range of 0.9 to 1.6 V vs. RHE at 20 mV s^{-1} scan rate in 1 M KOH. Typical cyclic voltammograms of GCE/$Zn_xFe_{3-x}O_4$, which show the lack of redox peaks in the chosen potential area, are shown in **Figure 3.5**. On a Ti support, cyclic voltammograms of Fe_3O_4 showed a similar appearance [58].

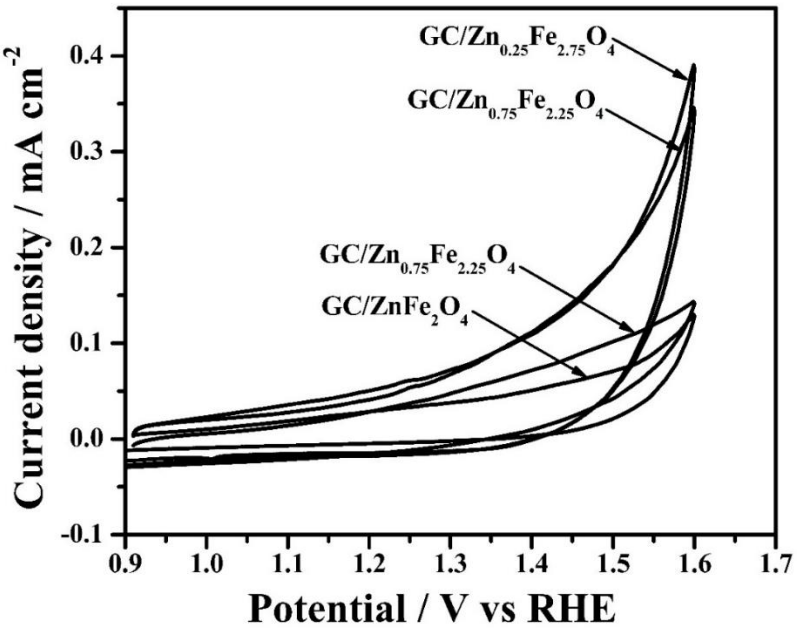

Figure 3.5. iR corrected cyclic voltammograms of GC/$Zn_xFe_{3-x}O_4$ electrode at 20 mV s^{-1} in 1 M KOH at 25 ºC.

Linear polarization (*i-E*) curves of GCE/$Zn_xFe_{3-x}O_4$ measured at 0.5 mV s^{-1} scan rate in the range of OER within 1.4 V to 1.8 V vs. RHE are shown in **Figure 3.6**. Again, the highest activity for OER, seen as the highest current density with lowest overpotential values is observed for GC/$Zn_{0.25}Fe_{2.75}O_4$, and the lowest current density with highest overpotential for GC/$ZnFe_2O_4$ electrode. The incorporation of zinc into the catalyst significantly enhances the anodic current density, signaling strong OER activity. This improvement is due to the formation of densely packed granular particles, which offer a favorable surface-to-bulk ratio, thereby promoting efficient electron and ion transfer and facilitating charge transport at the interface [59]. Additionally, the presence of zinc influences the grain boundaries (areas where different crystal grains converge and can obstruct charge carrier movement) [60]. The reduction in the number and impact of these grain boundaries due to zinc substitution leads to improved charge

transport and higher current density. Furthermore, substituting zinc enhances the electronic and chemical interaction among the cations. Zinc, with its lower resistivity, enhances electron transport by reducing ion diffusion pathways and accelerating water molecule adsorption, ultimately boosting the electrode's performance in the OER [61]. The loss of catalytic activity beyond Zn = 0.25 might be due to collapsing the structural morphology or by lowering oxygen vacancies [62].

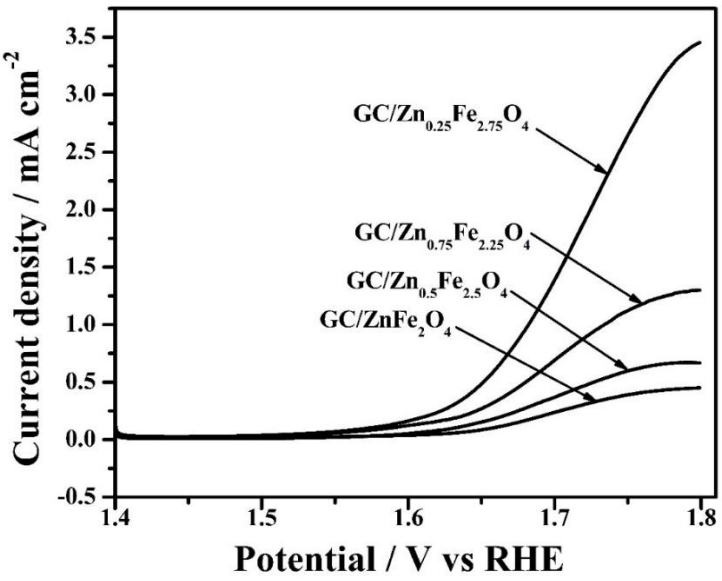

Figure 3.6. iR corrected linear polarization curves for GC/$Zn_xFe_{3-x}O_4$ electrodes at 0.5 mV s^{-1} scan rate in 1 M KOH at 25 ºC.

The Tafel polarization curve was used to determine the electrocatalytic activity in terms of log current density (log *j*) at overpotential (η). The formal overpotential, commonly referred to as the anodic overpotential, was established by the relationship $\eta = E - E_{O2/OH^-}$ [63], where *E* and E_{O2/OH^-} = 0.303 V vs. Hg/HgO, are the applied potential across the electrocatalyst/1 M KOH interface and the theoretical equilibrium Nernst potential vs. Hg/HgO in 1 M KOH at 25

°C, respectively. The overpotential was further calculated from the **Equation 1.19** after converting the potentials to RHE which is already discussed in **Chapter 1**.

The lowest overpotential is found for GC/$Zn_{0.25}Fe_{2.75}O_4$ electrode because of the faster electron transfer process at the interface and hence higher electrocatalytic activity [64]. **Table 3.3** lists the kinetic parameters of the prepared electrodes.

Table 3.3. Electrode kinetic parameters for OER on GC/$Zn_xFe_{3-x}O_4$ ($0 \leq x \leq 1$) electrodes in 1 M KOH at 25 °C.

Catalyst	**Overpotential (mV) at 1 mA cm^{-2}**	**Current density at E = 893 mV (mA cm^{-2})**			**C_{dl} (μF cm^{-2})**	**R_f**	**ECSA (cm^2)**	**Tafel Slope (mV dec^{-1})**
		j_{app}	**j_{true}**	**$j_{specific}$**				
$Zn_{0.25}Fe_{2.75}O_4$	480	3.4	0.44	3.4	309.5	7.7	0.539	107
$Zn_{0.5}Fe_{2.5}O_4$	590 (0.67 mA cm^{-2})	0.67	0.335	0.67	80	2	0.14	112
$Zn_{0.75}Fe_{2.25}O_4$	530	1.3	0.16	1.3	325.5	8.1	0.569	137
$ZnFe_2O_4$	596 (0.45 mA cm^{-2})	0.45	0.3	0.45	59.5	1.5	0.104	143

Moreover, electrode having lowest overpotential shows the highest current density that implies the better electrocatalytic activity among all the other prepared stoichiometrics. To normalize the electrode roughness and material loading on the substrate, the activity was also calculated in terms of true current density and current density per mg (specific current density) [65]. Apparent current density (j_{app}), true current density (j_{true}) and specific current density (j_{spec}) values, together with the estimated values of overpotential (at denoted current densities) for four prepared zinc ferrite samples are listed in **Table 3.3** (calculated from different plots of other catalysts shown in **Figure 3.7, 3.8, 3.9, and 3.10**). Either apparent current density (j_{app}) or true current density (j_{true}), normalized by the geometric surface area of the electrode or the oxide roughness factor, could be used to represent the rate of electrochemical oxygen evolution.

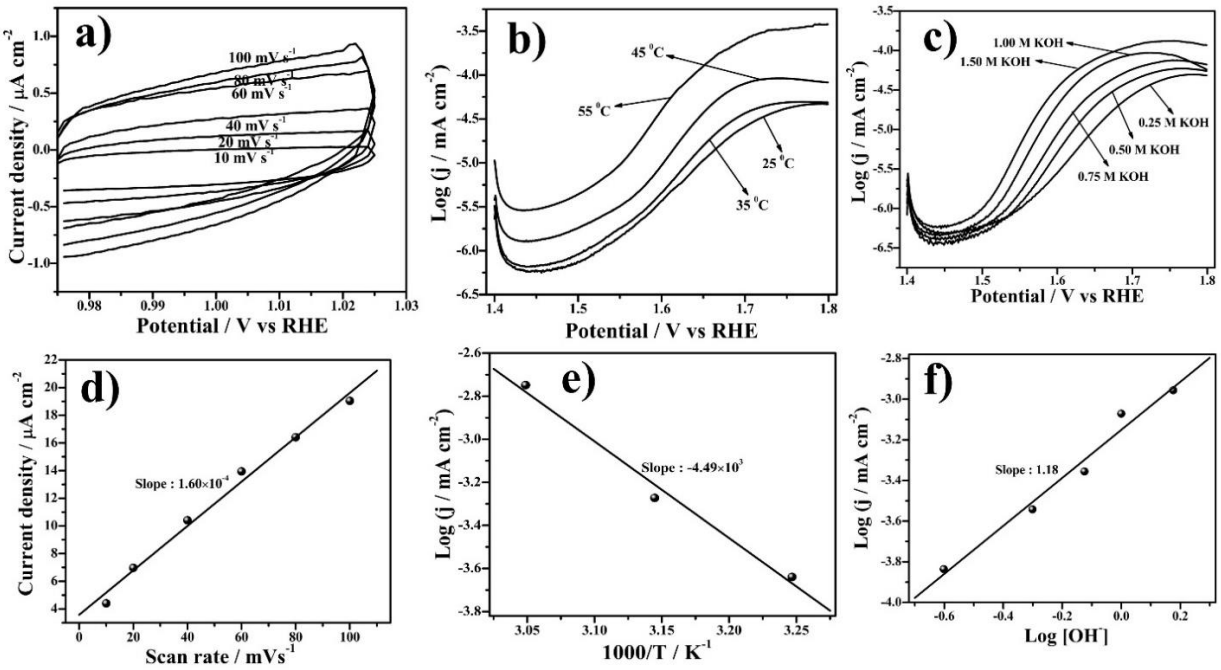

Figure 3.7. GC/$Zn_{0.5}Fe_{2.5}O_4$; **a)** Cyclic voltammograms in non-faradaic region at different scan rates in 1 M KOH at 25 °C, **b)** Tafel polarization curves at different temperatures at a scan rate of 0.5 mV s^{-1}, **c)** Tafel polarization curves at different concentrations at a scan rate of 0.5 mV s^{-1}, **d)** C_{dl} plot, **e)** Arrhenius plot at 1.6 V vs. RHE, **f)** order of reaction.

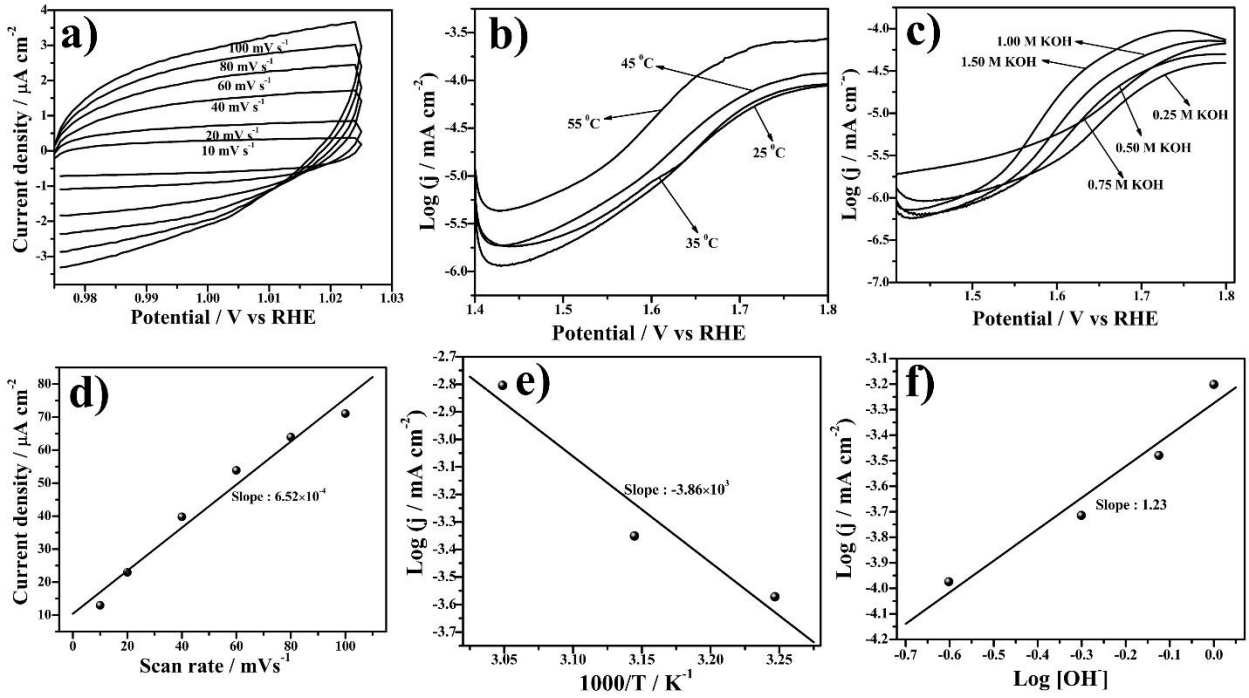

Figure 3.8. GC/$Zn_{0.75}Fe_{2.25}O_4$; **a)** Cyclic voltammograms in non-faradaic region at different scan rates in 1 M KOH at 25 °C, **b)** Tafel polarization curves at different temperatures at a scan rate of 0.5 mV s^{-1}, **c)** Tafel polarization curves at different concentrations at a scan rate of 0.5 mV s^{-1}, **d)** C_{dl} plot, **e)** Arrhenius plot at 1.6 V vs. RHE, **f)** order of reaction.

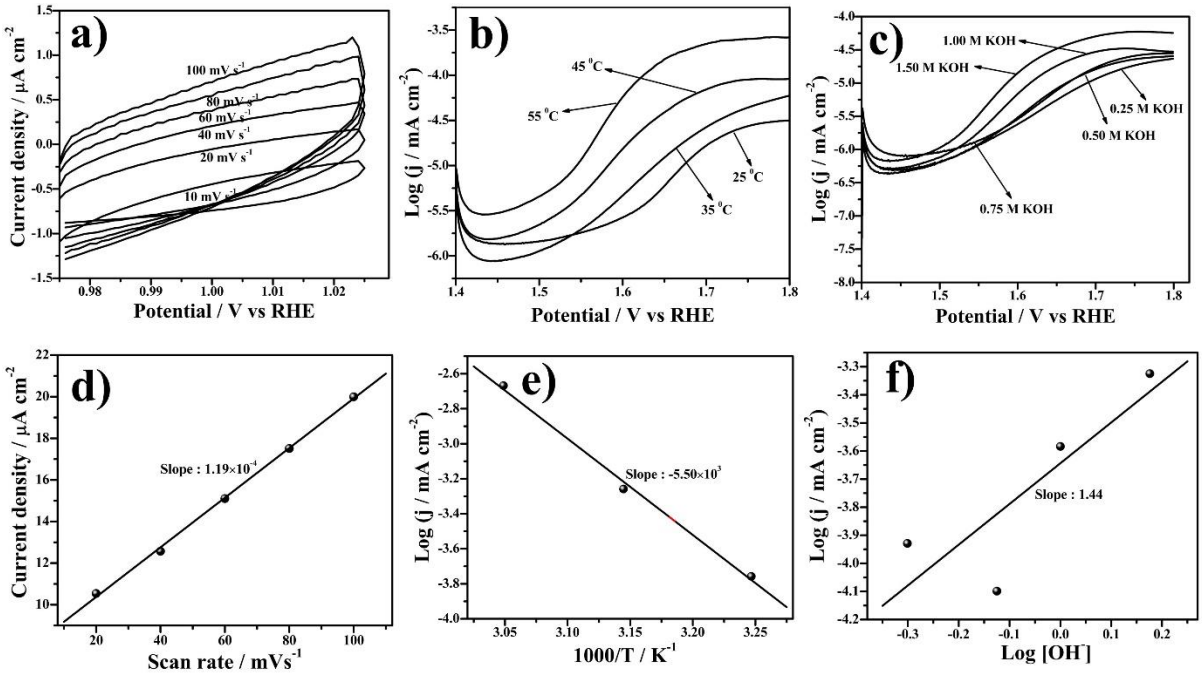

Figure 3.9. GC/$ZnFe_2O_4$; **a)** Cyclic voltammograms in non-faradaic region at different scan rates in 1 M KOH at 25 °C, **b)** Tafel polarization curves at different temperatures at a scan rate of 0.5 mV s^{-1}, **c)** Tafel polarization curves at different concentrations at a scan rate of 0.5 mV s^{-1}, **d)** C_{dl} plot, **e)** Arrhenius plot at 1.6 V vs. RHE, **f)** order of reaction.

By conducting cyclic voltammetry experiments in 1 M KOH at various scan rates within the potential region of 0.975 to 1.025 V (vs. RHE) at 25 °C, the surface roughness factor (R_f) of each oxide electrode was ascertained by calculating double layer capacitance. According to **Figure 3.5**, only capacitive currents due to double-layer charging-discharging predominate in this potential region. Representative cyclic voltammograms at varying scan rates and a plot of current density vs. scan rate are given in **Figure 3.10 (a) and (b)**, respectively. By assuming the double layer capacitance value of a smooth oxide surface equal to 40 μF cm^{-2}, the oxide roughness factors (R_f) of Zn ferrite samples were determined (From

Equation 1.24 in **Chapter 1**) [66]. Additionally, electrochemically active surface area was determined that tells us about the active sites during OER. R_f, together with C_{dl} **(**From **Equation 1.23** in **Chapter 1)** and ESCA values **(**From **Equation 1.22** in **Chapter 1)**, are also listed in **Table 3.3.**

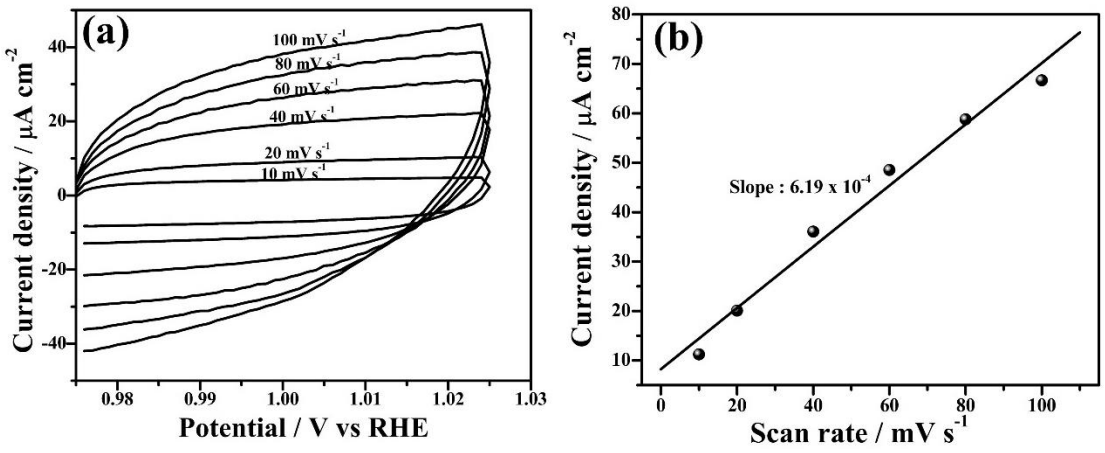

Figure 3.10. a) Cyclic voltammograms in non-faradaic region of GC/$Zn_{0.25}Fe_{2.75}O_4$ electrode at different scan rates in 1 M KOH at 25 ºC and **b)** capacitive current density vs. scan rate plot of GC/$Zn_{0.25}Fe_{2.75}O_4$ electrode.

Tafel polarization curves are shown in **Figure 3.11**. The Tafel slope, which is a measure of catalytic activity, was calculated using the analytical Tafel equation **(**From **Equation 1.21** in **Chapter 1)** [67]. Among all stoichiometrics of spinel ferrite, just $Zn_{0.25}Fe_{2.75}O_4$ coated on GCE showed the best electrocatalytic activity with lowest Tafel slope 107 mV dec^{-1} that indicates faster kinetics for OER. The obtained values of Tafel slopes are given in the **Table 3.3.**

The Tafel slope of $Zn_{0.25}Fe_{2.75}O_4$ is lower than that of other samples, suggesting high improvement in electrocatalytic activity. Changes in the electrical and magnetic characteristics

of the oxide catalyst cause an increase in electrocatalytic activity when metal ions are substituted in the Fe_3O_4 lattice [68]. Additionally, Iwakura *et al.* discovered that metal substitution in the Fe_3O_4 lattice increased saturation magnetization [69,70]. They also noticed that when Bohr magneton levels rose, so did the electrocatalytic activity for oxygen evolution reaction.

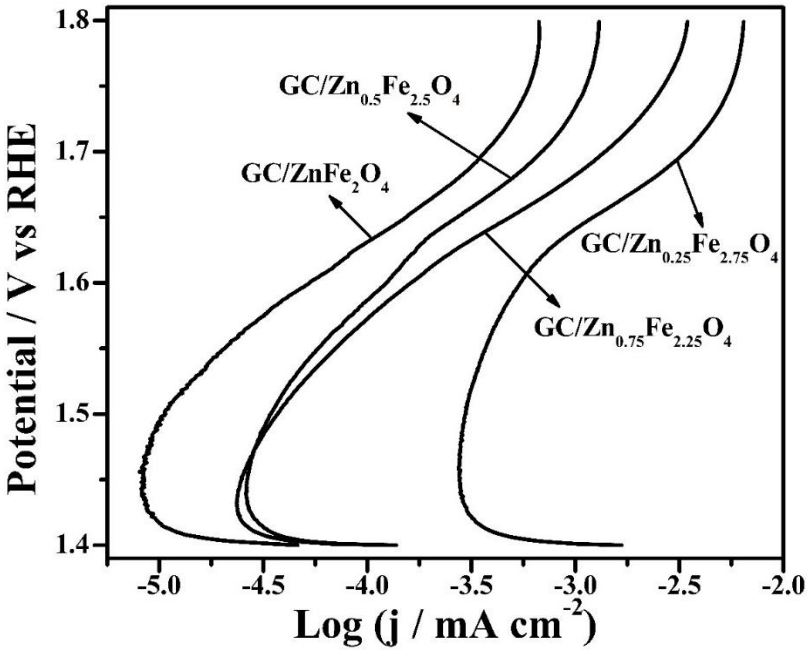

Figure 3.11. Tafel polarization curves of $GC/Zn_xFe_{3-x}O_4$ electrodes in 1 M KOH at 25 °C: **a)** $Zn_{0.25}Fe_{2.75}O_4$, **b)** $Zn_{0.75}Fe_{2.25}O_4$, **c)** $Zn_{0.5}Fe_{2.5}O_4$, **d)** $ZnFe_2O_4$.

To explain the reaction mechanism, the anodic Tafel polarization curves of $GC/Zn_xFe_{3-x}O_4$ electrodes were recorded at various KOH concentrations (0.25 M - 1.5 M), maintaining the medium-ionic strength constant (μ = 1.5), in order to determine the order of reaction (p) with regard to $[OH^-]$ **(Figure 3.12 (a))**. When determining the value of reaction order, the slope of the log j vs. log $[OH^-]$ plot **(Figure 3.12 (b))** across the oxide film/KOH interface at the

lower overpotential region particularly at potentials 1.55 V, 1.60 V, and 1.65 V vs. RHE was measured, and observed to be almost 2. This confirms the $4e^-$ OER mechanism in strongly alkaline medium [71].

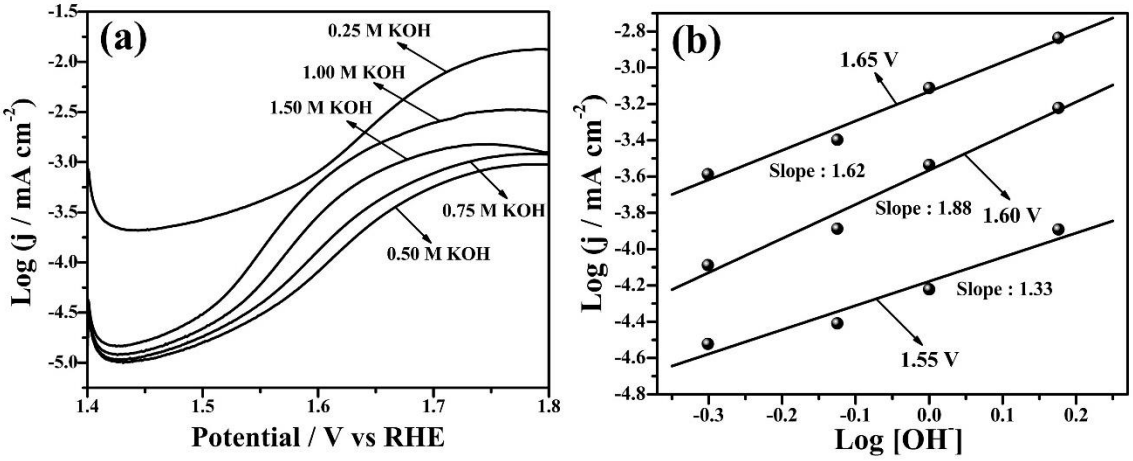

Figure 3.12. a) Tafel polarization curves of $Zn_{0.25}Fe_{2.75}O_4$ at different concentrations of KOH and 25 °C; **b)** plots of log j vs. log [OH^-].

Figure 3.13 shows Bode plots of $Zn_{0.25}Fe_{2.75}O_4$ recorded in the frequency range of 100 kHz to 1 Hz, at the constant potential of 0.95 V vs. RHE. Any contribution from a faradaic process is observed to be minimal at this potential [65]. The measured impedance spectra of interface was analyzed by fitting appropriate Randles circuit, R(Q(R(C(R(RW)))))(CR). The agreement between measured and simulated data was excellent. The chi-squared value of 10^{-4} speaks for the quality of the model [72].

The first part of Bode plots at the highest frequencies corresponds to the solution resistance of the electrolyte, R_s, and the second part at other frequencies shows mainly capacitive impedance response, as is expected for the electrode at potentials without faradaic

reaction(s). In that a case, the impedance due to double layer charging/discharging would dominate in the impedance spectrum. The corresponding phase angles in **Figure 3.13**, however, are much lower than expected -90°, which is usually related to not ideal electrode response due to interfacial irregularities such as porosity, roughness, and geometry [43,44], or possible influence of some other impedance. A clear deep in the phase angle response seen at low frequencies suggests a possible contribution of some additional impedance (resistive-capacitive combination due to oxide film perhaps) which parameters could eventually be estimated by curve fitting procedure of a proper model [74]. The capacitance value roughly estimated from the impedance magnitude |Z| of 500 Ω cm^2 at 1 Hz is 318 μF cm^{-2}, which is good agreement with C_{dl} value in **Table 3.3** for $Zn_{0.25}Fe_{2.75}O_4$.

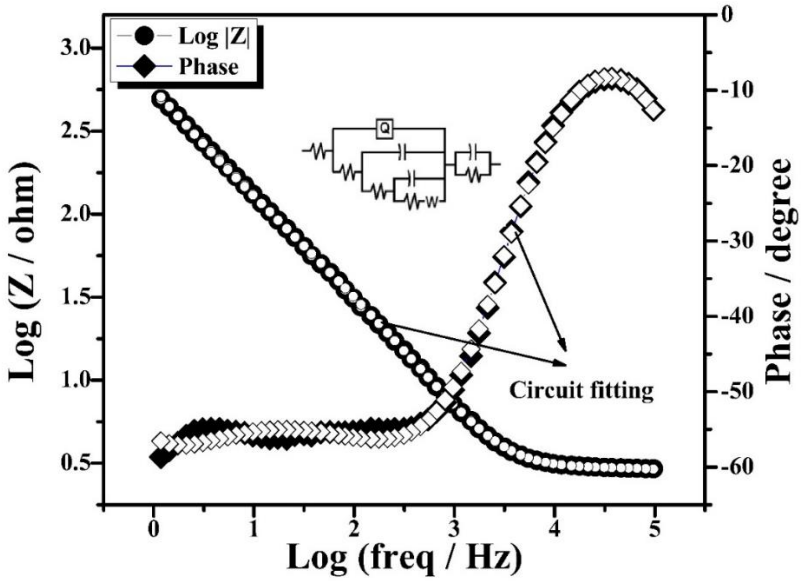

Figure 3.13. Typical Bode plot: $Zn_{0.25}Fe_{2.75}O_4$ in 1 M KOH at 0.95 V vs. RHE.

The simulated values of circuit parameters are given under the **Table 3.4**.

Table 3.4. Circuit Parameters

Catalysts	R	Q	Q	R	C	R	R	W	C	R
$Zn_{0.25}Fe_{2.75}O_4$	0.01	1.22 e^{-6}	0.99	2.88	2.06 e^{-6}	1.67	2.39	0.001	0.007	69.8
$Zn_{0.5}Fe_{2.5}O_4$	0.42	9.98 e^{-5}	0.79	3.29	7.61 e^{-6}	0.64	4.28	6.91	0.001	47.3
$Zn_{0.75}Fe_{2.25}O_4$	0.01	2.27 e^{-7}	0.94	2.72	1.87 e^{-5}	1.14	1.05	0.001	0.007	74.3
$ZnFe_2O_4$	0.27	3.08 e^{-5}	0.80	2.85	1.16 e^{-5}	0.57	2.03	9.48	0.001	157

Zn ferrite electrodes were tested for the measurement of standard electrochemical activation energies ($\Delta H_{el}^{0\neq}$), entropies ($\Delta S^{0\neq}$), and enthalpies ($\Delta H^{0\neq}$) in order to understand the impact of temperature on OER. With this goal in mind, anodic polarization curves were recorded in 1 M KOH at various temperatures ranging from 25 ºC to 55 ºC **(Figure 3.14 (a))**. For this purpose, Tafel polarization curves were recorded in the potential range of 1.4 V to 1.8 V vs. RHE at a scan rate of 0.5 mV s^{-1} at different temperatures. The temperature of the reference electrode was maintained constant during conducting of this experiment (25 ºC). For each curve, current density data was recorded for a certain potential (1.60 V and 1.65 V vs. RHE), and an Arrhenius plot of log j vs. 1/T **(Figure 3.14 (b))** was created. The result of

calculating the slopes of straight lines produced in the Arrhenius plots to determine values of $\Delta H_{el}^{0\neq}$ are shown in **Table 3.5.**

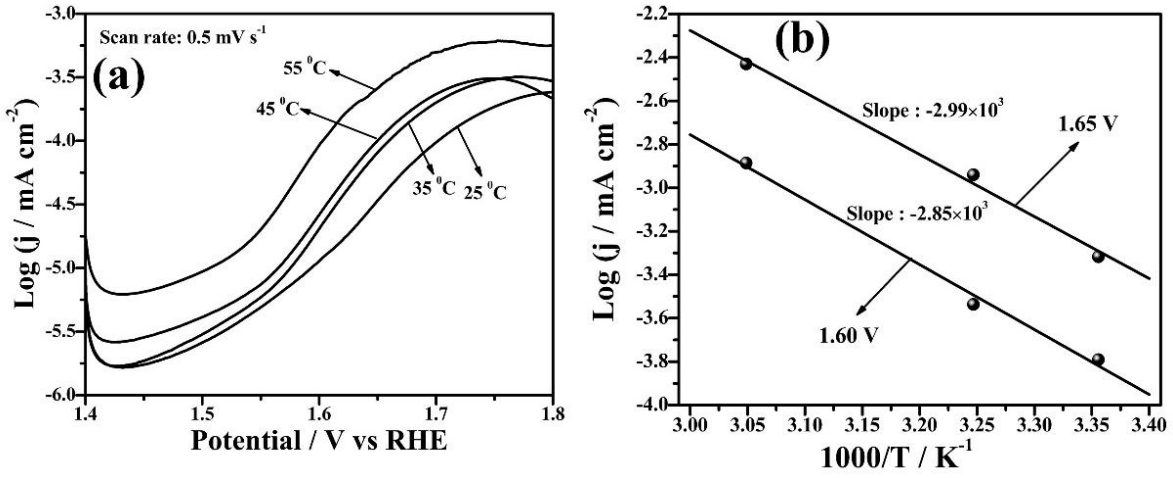

Figure 3.14. a) iR corrected Tafel polarization curves (at scan rate of 0.5 mV s^{-1}) of $Zn_{0.25}Fe_{2.75}O_4$ at different temperatures; **b)** Arrhenius plots for GC/$Zn_{0.25}Fe_{2.75}O_4$.

As anticipated, $Zn_{0.25}Fe_{2.75}O_4$ has a lower electrochemical activation energy value than any other synthesized Zn ferrite sample of different stoichiometry. The average value of calculated transfer coefficient (α) using the **Equation 1.28 (**From **Chapter 1)**, $\alpha = 2.303RT/bF$ was quite close to one. Using the **Equations 1.27 and 1.29 (**From **Chapter 1)**, other thermodynamic parameters, such as standard enthalpy of activation ($\Delta H^{0\neq}$), and standard entropy of activation ($\Delta S^{0\neq}$) were determined.

$$\Delta H_{el}^{0\neq} = \Delta H^{0\neq} - \alpha F \eta \qquad \textbf{(1.27)}$$

$$\Delta S^{0\neq} = 2.3R\,[\log j + \Delta H_{el}^{0\neq} / 2.3RT - \log (nF\omega C_{OH^-})] \qquad \textbf{(1.29)}$$

The Tafel slope (in mV dec^{-1}) is calculated from the polarization curve recorded at various temperatures, and R, F, and T are the gas constant, the Faraday constant, and absolute temperature, respectively. The Boltzmann constant (k_B) and Planck's constant (h) are two constants that make up the frequency term ω, respectively. The very negative value of $\Delta S^{0\neq}$ seen in **Table 3.5**, illustrates the adsorption events that precede the electrochemical production of oxygen.

Table 3.5. Thermodynamic parameters of OER on GC/$Zn_xFe_{3-x}O_4$ ($0 \leq x \leq 1.0$) electrodes in 1 M KOH.

Catalyst	**Standard electrochemical energy of activation ($\Delta H_{el}^{0\neq}$) (kJ mol^{-1})**	**Standard electrochemical entropy of activation ($-\Delta S_{el}^{0\neq}$) (J $K^{-1}mol^{-1}$)**	**Transfer coefficient (α)**	**Standard enthalpy of activation ($\Delta H^{0\neq}$) (kJ mol^{-1})**
$Zn_{0.25}Fe_{2.75}O_4$	54.22	74.96	0.70	92.36
$Zn_{0.5}Fe_{2.5}O_4$	85.98	172.16	0.65	120.24
$Zn_{0.75}Fe_{2.25}O4$	73.87	136.12	0.48	98.37
$ZnFe_2O_4$	105.28	237.12	0.56	135.3

Table 3.5 lists average values of these thermodynamic parameters [75]. The slope of Arrhenius plot (log *j* versus 1/T) was used to compute the value of $\Delta H_{el}^{0\neq}$, and the reaction entropy in each instance is strongly negative, confirming that electrochemical oxygen evolution happens *via* adsorption of reactive intermediate species. These parameters of other prepared catalysts were calculated by same manner.

3.5.3. Stability and durability

Beyond just high catalytic activity, a catalyst must also demonstrate exceptional stability for practical applications and commercialization. Evaluating the long-term stability and durability of the electrocatalyst is essential to ensure its suitability for real-world use. To this end, the stability of the GC/$Zn_{0.25}Fe_{2.75}O_4$ electrode was rigorously tested through prolonged chronopotentiometry in a 1 M KOH electrolyte. The chronopotentiometry results in **Figure 3.15** revealed that the electrode maintained a steady potential profile even after 6 hours of continuous operation, suggesting that its activity remained unaffected by the formation of gas bubbles.

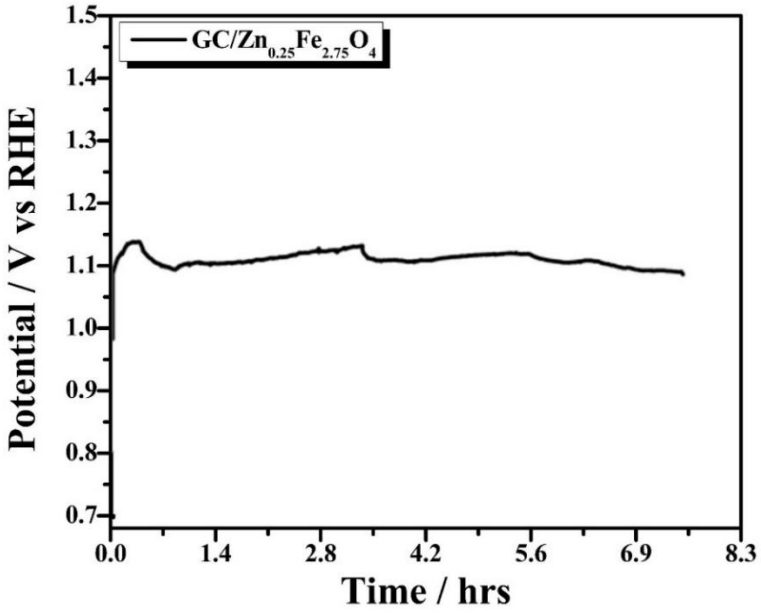

Figure 3.15. Chronopotentiometry test at constant current 1 mA cm^{-2}.

To further assess the durability, SEM imaging was conducted on the GC/$Zn_{0.25}Fe_{2.75}O_4$ electrode surface after the stability tests. The comparison with the fresh electrode revealed that the $Zn_{0.25}Fe_{2.75}O_4$ structure retained its surface morphology, with no visible structural degradation **(Figure 3.16)**. This observation underscores the electrode's exceptional structural integrity during OER performance, highlighting its potential for long-term operational stability and reliability. The preserved surface and structural stability affirm that the GC/$Zn_{0.25}Fe_{2.75}O_4$ electrode can sustain its performance under prolonged operational conditions, making it a promising candidate for practical applications.

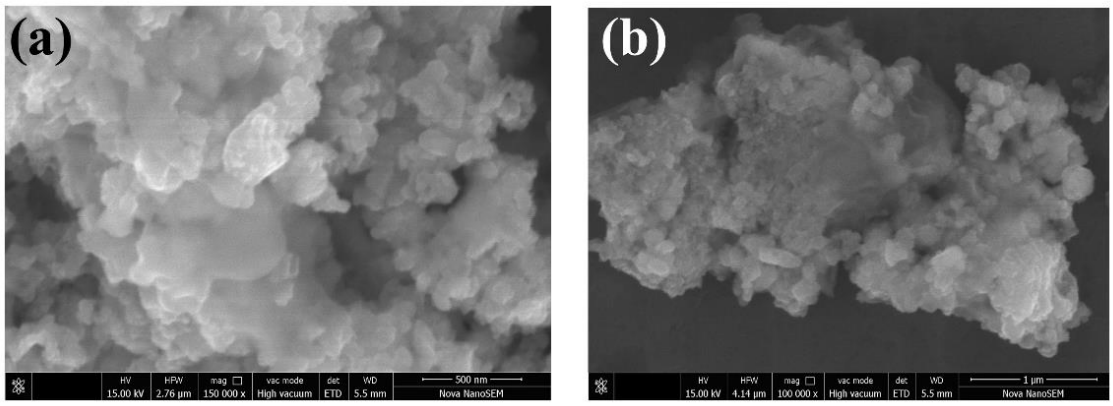

Figure 3.16. FE-SEM images of $Zn_{0.25}Fe_{2.75}O_4$; **a)** before stability test, **b)** after stability test.

3.5.4. Spectro-electrochemical analysis

It is interesting to note that UV-vis–NIR spectroscopy experiments conducted under OER circumstances have shown a rise in absorbance with applied voltage at the onset potential in the region of OER. Conway conducted the first investigation onto the impact of oxidized species on OER in the late 1950s. He found that the evolution of oxygen occurred concurrently with the potential decay from OER-relevant potentials to open-circuit potentials, indicating that oxidized states could be reduced to form molecular oxygen [76]. Oxo species on nearby Zn centers may chemically interact to form molecular oxygen, following a similar process to the OER predicted on Co in phosphate electrolyte [77–79] and CoOOH [80,81]. *Operando* UV-vis spectroscopy measurements were carried out to investigate the mechanism for OER and explain the activity patterns [82]. **Figure 3.17** depicts the *operando* UV-Vis spectroscopy before and during the cyclic voltammetry for the $Zn_{0.25}Fe_{2.75}O_4$ electrode performed at 25 ºC in 1 M KOH at scan rate of 20 mV s^{-1}, respectively. Upon stepping the electrode potential from 1.6 V to 1.8 V vs. RHE in 0.1 V increments, the formation of absorption peaks from 300 - 440

nm and a small peak from 850 - 900 nm were observed, and these absorbance peaks broadened and intensified with increase of applied potential. These may correspond to FeOOH species [83] when O_2 evolution is proceeding on the electrode.

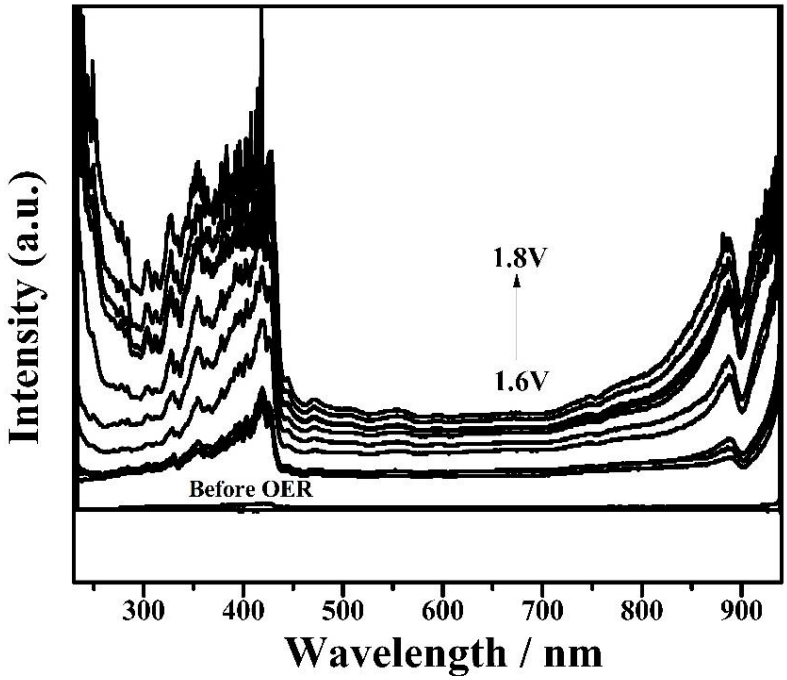

Figure 3.17. *Operando* UV-vis spectra during cyclic voltammetry at scan rate of 20 mV s^{-1}.

3.6. Conclusion

The characteristics of four synthesized samples of Zn ferrite ($Zn_xFe_{3-x}O_4$) with different stoichiometry ($0 \leq x \leq 1.0$) were evaluated up to the point of their possible use as electrocatalysts for active oxygen evolution processes in an alkaline medium (1 M KOH). According to the results of the performed experiments, zinc ferrites may be produced inexpensively and easily by auto combustion utilizing egg ovalbumin, resulting in nano-sized oxides that have greater spinel phase crystallinity. Tafel slope is found to be minimum for

$Zn_{0.25}Fe_{2.75}O_4$, for which the maximum electrocatalytic activity towards OER in an alkaline medium and nearly 2nd order kinetics is observed for the OER process. Among all four samples with different stoichiometry, $Zn_{0.25}Fe_{2.75}O_4$ showed the lowest standard electrochemical energy of activation which supports our findings. *Operando* spectro-electrochemical study revealed the active intermediates of OER, *i.e*., formation of absorption peaks from 300 - 440 nm that corresponds to FeOOH species. Further exploration in NIR region is needed to understand the role of redox active sites. The study showed that more than one redox species is forming during the OER which are responsible for electrocatalytic activity of $Zn_xFe_{3-x}O_4$ and the absorbance intensity is maximum for x=0.25 ($Zn_{0.25}Fe_{2.75}O_4$). For a comprehensive view from the catalyst to its surface, combining the presently known *operando* characterization approaches might be taken into consideration.

For improved real-time observation, it is also desirable to investigate novel approaches or improve current ones. A catalyst's stability is a crucial consideration when evaluating its OER performance together with its activity since stable catalysts are necessary for long-term catalysis under severe corrosive conditions. Creating a catalyst with great stability and activity is often difficult. Due to their negative correlation, stability and activity must sometimes be compromised [84]. It's crucial to use a logical measure to evaluate the stability of electrocatalysts. Activity-stability factor (ASF) was used by Markovic and coworkers as a standard measure to assess how well oxide materials performed for OER in acid. A higher ASF value corresponds to greater OER performance at a given overpotential [85]. Furthermore, these materials may be employed as electrode materials for energy storage devices and other

applications. Using OER catalysts, large-scale practical water splitting operations may be carried out, supplying the clean and efficient energy which has been generally required.

3.7. References

[1] D. Ramimoghadam, S. Bagheri, S.B.A. Hamid, Progress in electrochemical synthesis of magnetic iron oxide nanoparticles, J. Magn. Magn. Mater. 368 (2014) 207–229. https://doi.org/10.1016/j.jmmm.2014.05.015.

[2] G. Liu, J. Gao, H. Ai, X. Chen, Applications and potential toxicity of magnetic iron oxide nanoparticles, Small. 9 (2013) 1533–1545. https://doi.org/10.1002/smll.201201531.

[3] M.G. Naseri, E.B. Saion, M. Hashim, A.H. Shaari, H.A. Ahangar, Synthesis and characterization of zinc ferrite nanoparticles by a thermal treatment method, Solid State Commun. 151 (2011) 1031–1035. https://doi.org/10.1016/j.ssc.2011.04.018.

[4] P. Gangopadhyay, R. Kesavamoorthy, S. Bera, P. Magudapathy, K.G.M. Nair, B.K. Panigrahi, S. V. Narasimhan, Optical absorption and photoluminescence spectroscopy of the growth of silver nanoparticles, Phys. Rev. Lett. 94 (2005). https://doi.org/10.1103/PHYSREVLETT.94.047403.

[5] K. Bogle, S. Dhole, V.B.- Nanotechnology, undefined 2006, Silver nanoparticles: synthesis and size control by electron irradiation, iopscience.iop.org. 17 (2006) 3204–3208. https://doi.org/10.1088/0957-4484/17/13/021.

[6] G. Maggioni, A. Vomiero, S. Carturan, C. Scian, G. Mattei, M. Bazzan, C. De Julián Fernández, P. Mazzoldi, A. Quaranta, G. Della Mea, Structure and optical properties of Au-polyimide nanocomposite films prepared by ion implantation, Appl. Phys. Lett. 85 (2004) 5712–5714. https://doi.org/10.1063/1.1829390.

[7] S. Neogi, U. Chowdhury, A.K. Chakraborty, J. Ghosh, Effect of mechanical milling on the structural and dielectric properties of BaTiO3 powders, Micro Nano Lett. 10 (2015) 109–114. https://doi.org/10.1049/mnl.2013.0751.

[8] S.H. Yu, T. Fujino, M. Yoshimura, Hydrothermal synthesis of ZnFe2O4 ultrafine particles with high magnetization, J. Magn. Magn. Mater. 256 (2003) 420–424. https://doi.org/10.1016/S0304-8853(02)00977-0.

[9] V.G. Morrison, S. A., Cahill, C. L., Carpenter, E. E., & Harris, Production Scaleup of Reverse Micelle Synthesis, Ind. Eng. Chem. Res. 2006 45 (3), 1217-1220. (n.d.). https://doi.org/10.1021/ie050886l.

[10] M.P. JF Hochepied, P Bonville, Nonstoichiometric Zinc Ferrite Nanocrystals: Syntheses and Unusual Magnetic Properties, J. Phys. Chem. B 2000 104 (5), 905-912. (n.d.). https://doi.org/10.1021/jp991626i.

[11] M.A. Gabal, R.M. El-Shishtawy, Y.M. Al Angari, Structural and magnetic properties of nano-crystalline NiZn ferrites synthesized using egg-white precursor, J. Magn. Magn. Mater. 324 (2012) 2258–2264. https://doi.org/10.1016/j.jmmm.2012.02.112.

[12] X. Liu, K. Li, C. Wu, Y. Zhou, C. Pei, Egg white-assisted preparation of inorganic functional materials: A sustainable, eco-friendly, low-cost and multifunctional method, Ceram. Int. 45 (2019) 23869–23889. https://doi.org/10.1016/j.ceramint.2019.08.152.

[13] M.A. Gabal, A.A. Al-Juaid, S. El-Rashed, M.A. Hussein, Synthesis and characterization of nano-sized CoFe2O4 via facile methods: A comparative study, Mater. Res. Bull. 89 (2017) 68–78. https://doi.org/10.1016/j.materresbull.2016.12.048.

[14] M.A. Gabal, Magnetic properties of NiCuZn ferrite nanoparticles synthesized using egg-white, Mater. Res. Bull. 45 (2010) 589–593. https://doi.org/10.1016/j.materresbull.2010.01.021.

[15] S. Maensiri, C. Masingboon, B. Boonchom, S. Seraphin, A simple route to synthesize nickel ferrite (NiFe2O4) nanoparticles using egg white, Scr. Mater. 56 (2007) 797–800. https://doi.org/10.1016/j.scriptamat.2006.09.033.

[16] Y.M. Al Angari, Electromagnetic properties of nanocrystalline Mn-Zn ferrite synthesized from spent Zn-C battery via Egg-white route, Int. J. Electrochem. Sci. 13 (2018) 12331–12339. https://doi.org/10.20964/2018.12.25.

[17] S. Dhara, P. Bhargava, A Simple Direct Casting Route to Ceramic Foams, J. Am. Ceram. Soc. 86 (2003) 1645–1650. https://doi.org/10.1111/J.1151-2916.2003.TB03534.X.

[18] M.A. Gabal, Effect of Mg substitution on the magnetic properties of NiCuZn ferrite nanoparticles prepared through a novel method using egg white, J. Magn. Magn. Mater. 321 (2009) 3144–3148. https://doi.org/10.1016/J.JMMM.2009.05.047.

[19] A.K. Singh, S. Kumar, B. Sen Yadav, A.K. Vishwakarma, N. Kumar, Evidence of oxygen evolution over sputtered zinc ferrite (ZnFe2O4) thin film by enhanced lattice oxygen participation, Appl. Phys. Lett. 123 (2023) 33902. https://doi.org/10.1063/5.0154955.

[20] R. Appiah-Ntiamoah, A.F. Baye, H. Kim, In Situ Electrochemical Formation of a Core-Shell ZnFe2O4@Zn(Fe)OOH Heterostructural Catalyst for Efficient Water Oxidation in Alkaline Medium, ChemElectroChem. 7 (2020) 3478–3486. https://doi.org/10.1002/celc.202000834.

[21] N.M. Malima, M.D. Khan, J. Choi, R.K. Gupta, N. Revaprasadu, Alloying normal and

inverse spinel (Zn–Co ferrite) nanostructures via direct precursor pyrolysis for enhanced supercapacitance and water splitting, Mater. Chem. Phys. 302 (2023) 127770. https://doi.org/10.1016/j.matchemphys.2023.127770.

[22] X. Liu, Z. Chang, L. Luo, T. Xu, X. Lei, J. Liu, X. Sun, Hierarchical Zn x Co3-xO4 nanoarrays with high activity for electrocatalytic oxygen evolution, Chem. Mater. 26 (2014) 1889–1895. https://doi.org/10.1021/cm4040903.

[23] Y. Gong, H. Pan, Z. Xu, Z. Yang, Y. Lin, M. Zhang, ACo2O4 (A=Ni, Zn, Mn) nanostructure arrays grown on nickel foam as efficient electrocatalysts for oxygen evolution reaction, Int. J. Hydrogen Energy. 43 (2018) 14360–14368. https://doi.org/10.1016/j.ijhydene.2018.06.025.

[24] W. Peng, G. Zheng, Y. Wang, S. Cao, Z. Ji, Y. Huan, M. Zou, X. Yan, Zn doped ZIF67-derived porous carbon framework as efficient bifunctional electrocatalyst for water splitting, Int. J. Hydrogen Energy. 44 (2019) 19782–19791. https://doi.org/10.1016/j.ijhydene.2019.05.101.

[25] L. Li, Y. Zhang, J. Li, W. Huo, B. Li, J. Bai, Y. Cheng, H. Tang, X. Li, Facile synthesis of yolk-shell structured ZnFe 2 O 4 microspheres for enhanced electrocatalytic oxygen evolution reaction, Inorg. Chem. Front. 6 (2019) 511–520. https://doi.org/10.1039/c8qi01191e.

[26] Y. Hu, X. Zhao, F. Li, Q. Dong, B. Wen, D. Sun, W. Liang, X. Lyu, Spherical ZnFe2O4 Nanoparticles on Nitrogen-Doped Graphene: A Synergistic Effect on Efficient Electrocatalytic Oxygen Evolution Reaction, ACS Appl. Energy Mater. 6 (2023) 9985–9993. https://doi.org/10.1021/acsaem.3c01571.

[27] S. Chakrabarty, A. Mukherjee, W.N. Su, S. Basu, Improved bi-functional ORR and OER catalytic activity of reduced graphene oxide supported ZnCo2O4 microsphere, Int. J. Hydrogen Energy. 44 (2019) 1565–1578. https://doi.org/10.1016/j.ijhydene.2018.11.163.

[28] S.D. Jituri, R.P. Nikam, V.J. Mane, S.B. Shaikh, C.D. Lokhande, S.H. Mujawar, Chemically synthesized ZnFe2O4electrodes for electrochemical oxygen evolution reaction and supercapacitor applications, J. Mater. Sci. Mater. Electron. 34 (2023) 1–13. https://doi.org/10.1007/s10854-023-11299-5.

[29] E. Mohammadpour, K. Asadpour-Zeynali, ZnFe2O4@ZnFe2S4 core-shell nanosheet on Ni foam as efficient and novel electrocatalyst for oxygen generation, Int. J. Hydrogen Energy. 46 (2021) 26940–26949. https://doi.org/10.1016/j.ijhydene.2021.05.183.

[30] T. Abe, M. Kaneko, Reduction catalysis by metal complexes confined in a polymer matrix, Prog. Polym. Sci. 28 (2003) 1441–1488. https://doi.org/10.1016/S0079-6700(03)00057-1.

[31] K. Murofushi, K. Ogawa, H. Suzuki, R. Sakamoto, O. Tomita, K. Kato, A. Yamakata, A. Saeki, R. Abe, Earth-abundant iron(iii) species serves as a cocatalyst boosting the multielectron reduction of IO3-/I-redox shuttle in Z-scheme photocatalytic water splitting, J. Mater. Chem. A. 9 (2021) 11718–11725. https://doi.org/10.1039/d1ta01703a.

[32] M. Higashi, K. Domen, R. Abe, Fabrication of an efficient BaTaO2N photoanode harvesting a wide range of visible light for water splitting, J. Am. Chem. Soc. 135 (2013) 10238–10241. https://doi.org/10.1021/ja404030x.

[33] S. Wang, A. Lu, C.J. Zhong, Hydrogen production from water electrolysis: role of catalysts, Nano Converg. 8 (2021) 1–23. https://doi.org/10.1186/S40580-021-00254-X/FIGURES/16.

[34] R.L. and Z.W. Dezhi Wang, Yuwen Song, Ting Guo, Construction of FeS2@MoS2 heterostructures for enhanced hydrogen evolution, Sustain. Energy Fuels, 2022,6, 2243-2248. (n.d.). https://doi.org/https://doi.org/10.1039/D2SE00262K.

[35] W.H. Huang, X.M. Li, X.F. Yang, H. Bin Zhang, F. Wang, J. Zhang, Highly efficient electrocatalysts for overall water splitting: mesoporous CoS/MoS2 with hetero-interfaces, Chem. Commun. 57 (2021) 4847–4850. https://doi.org/10.1039/D1CC01578H.

[36] G. Zhao, K. Rui, S.X. Dou, W. Sun, Boosting electrochemical water oxidation: the merits of heterostructured electrocatalysts, J. Mater. Chem. A. 8 (2020) 6393–6405. https://doi.org/10.1039/D0TA00708K.

[37] Y. Lee, J. Suntivich, K.J. May, E.E. Perry, Y. Shao-Horn, Synthesis and activities of rutile IrO 2 and RuO 2 nanoparticles for oxygen evolution in acid and alkaline solutions, J. Phys. Chem. Lett. 3 (2012) 399–404. https://doi.org/10.1021/JZ2016507/SUPPL_FILE/JZ2016507_SI_001.PDF.

[38] A. Grimaud, O. Diaz-Morales, B. Han, W.T. Hong, Y.L. Lee, L. Giordano, K.A. Stoerzinger, M.T.M. Koper, Y. Shao-Horn, Activating lattice oxygen redox reactions in metal oxides to catalyse oxygen evolution, Nat. Chem. 2017 95. 9 (2017) 457–465. https://doi.org/10.1038/nchem.2695.

[39] A. Grimaud, K.J. May, C.E. Carlton, Y.L. Lee, M. Risch, W.T. Hong, J. Zhou, Y. Shao-Horn, Double perovskites as a family of highly active catalysts for oxygen

evolution in alkaline solution, Nat. Commun. 2013 41. 4 (2013) 1–7. https://doi.org/10.1038/ncomms3439.

[40] J. Hwang, R.R. Rao, L. Giordano, Y. Katayama, Y. Yu, Y. Shao-Horn, Perovskites in catalysis and electrocatalysis, Science (80-.). 358 (2017) 751–756. https://doi.org/10.1126/science.aam7092.

[41] K. Kawashima, R.A. Márquez, Y.J. Son, C. Guo, R.R. Vaidyula, L.A. Smith, C.E. Chukwuneke, C.B. Mullins, Accurate Potentials of Hg/HgO Electrodes: Practical Parameters for Reporting Alkaline Water Electrolysis Overpotentials, ACS Catal. 13 (2023) 1893–1898. https://doi.org/10.1021/ACSCATAL.2C05655/ASSET/IMAGES/LARGE/CS2C05655_0003.JPEG.

[42] J.L.H. Chau, M.K. Hsu, C.C. Kao, Microwave plasma synthesis of Co and SiC-coated Co nanopowders, Mater. Lett. 60 (2006) 947–951. https://doi.org/10.1016/j.matlet.2005.10.054.

[43] R.N. Singh, J.P. Singh, B. Lal, M.J.K. Thomas, S. Bera, New NiFe2-xCrxO4 spinel films for O2 evolution in alkaline solutions, Electrochim. Acta. 51 (2006) 5515–5523. https://doi.org/10.1016/j.electacta.2006.02.028.

[44] J.-F.K. R.N. Singh,J.P. Pandey,N.K. Singh,B. Lal,P. Chartier, Sol-gel derived spinel M x Co3−x O4 (M=Ni, Cu; 0≤x≤1) films and oxygen evolution, Electrochim. Acta. (n.d.). https://doi.org/https://doi.org/10.1016/S0013-4686(99)00413-2.

[45] M.A. Ahmed, E. Ateia, S.I. El-Dek, Spectroscopic analysis of ferrite doped with different rare earth elements, Vib. Spectrosc. 30 (2002) 69–75. https://doi.org/10.1016/S0924-2031(02)00040-1.

[46] B.J. Evans, S.S. Hafner, Mössbauer resonance of Fe57 in oxidic spinels containing Cu and Fe, J. Phys. Chem. Solids. 29 (1968) 1573–1588. https://doi.org/10.1016/0022-3697(68)90100-5.

[47] M. Wang, Z. Ai, L. Zhang, Generalized preparation of porous nanocrystalline zoned2O 4 superstructures from zinc ferrioxalate precursor and its superparamagnetic property, J. Phys. Chem. C. 112 (2008) 13163–13170. https://doi.org/10.1021/JP804009H.

[48] R. Rameshbabu, R. Ramesh, S. Kanagesan, A. Karthigeyan, S. Ponnusamy, Synthesis and study of structural, morphological and magnetic properties of ZnFe2O4 nanoparticles, J. Supercond. Nov. Magn. 27 (2014) 1499–1502. https://doi.org/10.1007/S10948-013-2466-Z/FIGURES/4.

[49] J.P. Singh, G. Dixit, R.C. Srivastava, P. Negi, H.M. Agrawal, R. Kumar, HRTEM and FTIR investigation of nanosized zinc ferrite irradiated with 100 MeV oxygen ions, Spectrochim. Acta - Part A Mol. Biomol. Spectrosc. 107 (2013) 326–333. https://doi.org/10.1016/j.saa.2012.12.095.

[50] A. Pradeep, P. Priyadharsini, G. Chandrasekaran, Structural, magnetic and electrical properties of nanocrystalline zinc ferrite, J. Alloys Compd. 509 (2011) 3917–3923. https://doi.org/10.1016/j.jallcom.2010.12.168.

[51] S. Bera, A.A.M. Prince, S. Velmurugan, P.S. Raghavan, R. Gopalan, G. Panneerselvam, S. V. Narasimhan, Formation of zinc ferrite by solid-state reaction and its characterization by XRD and XPS, J. Mater. Sci. 36 (2001) 5379–5384. https://doi.org/10.1023/A:1012488422484.

[52] M. Deepty, C. Srinivas, E.R. Kumar, N.K. Mohan, C.L. Prajapat, T.V.C. Rao, S.S. Meena, A.K. Verma, D.L. Sastry, XRD, EDX, FTIR and ESR spectroscopic studies of co-precipitated Mn–substituted Zn–ferrite nanoparticles, Ceram. Int. 45 (2019) 8037–8044. https://doi.org/10.1016/j.ceramint.2019.01.029.

[53] M.A. Valenzuela, P. Bosch, J. Jiménez-Becerrill, O. Quiroz, A.I. Páez, Preparation, characterization and photocatalytic activity of ZnO, Fe2O3 and ZnFe2O4, J. Photochem. Photobiol. A Chem. 148 (2002) 177–182. https://doi.org/10.1016/S1010-6030(02)00040-0.

[54] L. Andjelković, M. Šuljagić, M. Lakić, D. Jeremić, P. Vulić, A.S. Nikolić, A study of the structural and morphological properties of Ni–ferrite, Zn–ferrite and Ni–Zn–ferrites functionalized with starch, Ceram. Int. 44 (2018) 14163–14168. https://doi.org/10.1016/j.ceramint.2018.05.018.

[55] A.F. Gross, M.R. Diehl, K.C. Beverly, E.K. Richman, S.H. Tolbert, Controlling magnetic coupling between cobalt nanoparticles through nanoscale confinement in hexagonal mesoporous silica, J. Phys. Chem. B. 107 (2003) 5475–5482. https://doi.org/10.1021/jp034240n.

[56] M.M. Vijatović Petrović, J.D. Bobić, H. Uršič, J. Banys, B.D. Stojanović, The electrical properties of chemically obtained barium titanate improved by attrition milling, J. Sol-Gel Sci. Technol. 67 (2013) 267–272. https://doi.org/10.1007/s10971-013-3075-9.

[57] H. Jalili, B. Aslibeiki, A.G. Varzaneh, V.A. Chernenko, The effect of magneto-crystalline anisotropy on the properties of hard and soft magnetic ferrite nanoparticles, Beilstein J. Nanotechnol. 10 (2019) 1348–1359. https://doi.org/10.3762/BJNANO.10.133.

[58] M.S. Al-Hoshan, J.P. Singh, A.M. Al-Mayouf, A.A. Al-Suhybani, M.N. Shaddad, Synthesis, physicochemical and electrochemical properties of nickel ferrite spinels obtained by hydrothermal method for the Oxygen Evolution Reaction (OER), Int. J. Electrochem. Sci. 7 (2012) 4959–4973.

[59] N.A. Khan, G. Rahman, S.Y. Chae, N. Yoon, A. ul H.A. Shah, S.A. Mian, Unraveling the Electrocatalytic Response of Zn-Substituted Nickel Ferrite for Overall Water Splitting, ACS Appl. Energy Mater. 7 (2024) 4960–4974. https://doi.org/10.1021/acsaem.4c00810.

[60] J.R.D. Santos, R.A. Raimundo, J.F.G. d. A. Oliveira, J. da S. Hortencio, F.J.A. Loureiro, D.A. Macedo, M.A. Morales, I. Gualandi, D. Tonelli, U.U. Gomes, Eco-friendly high entropy oxide rock-salt type structure for oxygen evolution reaction obtained by green synthesis, J. Electroanal. Chem. 961 (2024) 118191. https://doi.org/10.1016/j.jelechem.2024.118191.

[61] G. Umapathy, G. Senguttuvan, L. John Berchmans, V. Sivakumar, Structural, dielectric and AC conductivity studies of Zn substituted nickel ferrites prepared by combustion technique, J. Mater. Sci. Mater. Electron. 27 (2016) 7062–7072. https://doi.org/10.1007/s10854-016-4664-5.

[62] S. Pal, U.P. Azad, A.K. Singh, D. Kumar, R. Prakash, Studies on some spinel oxides based electrocatalysts for oxygen evolution and capacitive applications, Electrochim. Acta. 320 (2019) 134584. https://doi.org/10.1016/j.electacta.2019.134584.

[63] R.N. Singh, J.P. Pandey, N.K. Singh, B. Lal, P. Chartier, J.F. Koenig, Sol-gel derived spinel MxCo3-xO4 (M = Ni, Cu; 0≤x≤1) films and oxygen evolution, Electrochim. Acta. 45 (2000) 1911–1919. https://doi.org/10.1016/S0013-4686(99)00413-2.

[64] J.R.D. Santos, R.A. Raimundo, T.R. Silva, V.D. Silva, D.A. Macedo, F.J.A. Loureiro, M.A.M. Torres, D. Tonelli, U.U. Gomes, Nanoparticles of Mixed-Valence Oxides MnXCO3-XO4 ($0 \leq X \leq 1$) Obtained with Agar-Agar from Red Algae (Rhodophyta) for Oxygen Evolution Reaction, Nanomaterials. 12 (2022) 3170. https://doi.org/10.3390/nano12183170.

[65] A.S. Chaddha, N.K. Singh, M. Malviya, A. Sharma, Birnessite-clay mineral couple in the rock varnish: a nature's electrocatalyst, Sustain. Energy Fuels. 6 (2022) 2553–2569. https://doi.org/10.1039/d2se00185c.

[66] B. Lal, Elctrocatalytic oxygen evolution reaction on Mg, Al and Fe doped spinel oxides, Indian J. Chem. -Section A. 60 (2021) 1303–1308. https://doi.org/10.56042/ijca.v60i10.48885.

[67] Z. Hu, L. Hao, F. Quan, R. Guo, Recent developments of Co3O4-based materials as catalysts for the oxygen evolution reaction, Catal. Sci. Technol. 12 (2022) 436–461. https://doi.org/10.1039/d1cy01688a.

[68] E. O'Sullivan, E.C.-C. chemical kinetics, undefined 1988, Reactions at metal oxide electrodes, Elsevier. (n.d.). https://doi.org/10.1016/S0069-8040(08)70017-7.

[69] H. Iwakura, C., Nishioka, M., & Tamura, Oxygen evolution on spinel-type ferrite film electrodes, Chem. Soc. japan. (n.d.). https://doi.org/Nippon Kagaku Kaishi, (7), 1136-1140.

[70] H. Iwakura, C., Nishioka, M., & Tamura, CORRELATION BETWEEN OXYGEN OVERVOLTAGE AND MAGNETIC PROPERTY OF SPINEL-TYPE FERRITE FILM ELECTRODES., Chem. Soc. japan. (n.d.). https://doi.org/Denki Kagaku, 49(8), 535-536.

[71] Y. Zhang, H. Zhang, A. Liu, C. Chen, W. Song, J. Zhao, Rate-Limiting O-O Bond Formation Pathways for Water Oxidation on Hematite Photoanode, J. Am. Chem. Soc. 140 (2018) 3264–3269. https://doi.org/10.1021/JACS.7B10979/ASSET/IMAGES/LARGE/JA-2017-10979E_0004.JPEG.

[72] Manisha Malviya, (8) Fuel cell application: composite electrodes, Manisha Malviya; Lambert Academic Publishers, Germany, 2011. ISBN 978-3-8473-3898-7. | Request PDF, Lambert Acad. Publ. (2011). https://doi.org/ISBN 978-3-8473-3898-7.

[73] P. Fiordiponti, G. Pistoia, An impedance study of polyaniline films in aqueous and organic solutions, Electrochim. Acta. 34 (1989) 215–221. https://doi.org/10.1016/0013-4686(89)87088-4.

[74] R. Schrebler, H. Gómez, R. Cordova, L.M. Gassa, J.R. Vilche, Study of the aniline oxidation process and characterization of Pani films by electrochemical impedance spectroscopy, Synth. Met. 93 (1998) 187–192. https://doi.org/10.1016/s0379-6779(97)04107-6.

[75] K.E. Heusler, E. Gileadi; electrode kinetics for chemists, chemical engineers and material scientists. VCH, Weinheim, New York, Basel, Cambridge, Tokyo 1993, ISBN 3-527-89561-2, 597 S., Preis: DM 189,-, Berichte der Bunsengesellschaft für Phys. Chemie. 98 (1994) 644–645. https://doi.org/10.1002/BBPC.19940980425.

[76] B.E. Conway, P.L. Bourgault, THE ELECTROCHEMICAL BEHAVIOR OF THE NICKEL – NICKEL OXIDE ELECTRODE: PART I. KINETICS OF SELF-DISCHARGE, Can. J. Chem. 37 (1959) 292–307. https://doi.org/10.1139/V59-038.

[77] D.K. Bediako, Y. Surendranath, D.G. Nocera, Mechanistic studies of the oxygen evolution reaction mediated by a nickel-borate thin film electrocatalyst, J. Am. Chem. Soc. 135 (2013) 3662–3674. https://doi.org/10.1021/ja3126432.

[78] Y. Surendranath, M.W. Kanan, D.G. Nocera, Mechanistic studies of the oxygen evolution reaction by a cobalt-phosphate catalyst at neutral pH, J. Am. Chem. Soc. 132 (2010) 16501–16509. https://doi.org/10.1021/JA106102B.

[79] C. Costentin, D.G. Nocera, Self-healing catalysis in water, Proc. Natl. Acad. Sci. U. S. A. 114 (2017) 13380–13384. https://doi.org/10.1073/PNAS.1711836114.

[80] A. Moysiadou, S. Lee, H.C.-J. of the A. Hsu, CS, U. 2020, Mechanism of oxygen evolution catalyzed by cobalt oxyhydroxide: cobalt superoxide species as a key intermediate and dioxygen release as a rate-determining step, ACS Publ. 142 (2020) 11901–11914. https://doi.org/10.1021/jacs.0c04867.

[81] L.P. Wang, T. Van Voorhis, Direct-coupling O2 bond forming a pathway in cobalt oxide water oxidation catalysts, J. Phys. Chem. Lett. 2 (2011) 2200–2204. https://doi.org/10.1021/JZ201021N.

[82] R.R. Rao, S. Corby, A. Bucci, M. García-Tecedor, C.A. Mesa, J. Rossmeisl, S. Giménez, J. Lloret-Fillol, I.E.L. Stephens, J.R. Durrant, Spectroelectrochemical Analysis of the Water Oxidation Mechanism on Doped Nickel Oxides, J. Am. Chem. Soc. 144 (2022) 7622–7633. https://doi.org/10.1021/JACS.1C08152/ASSET/IMAGES/LARGE/JA1C08152_0005.JPEG.

[83] H. Mashiko, K. Yoshimatsu, T. Oshima, A. Ohtomo, Fabrication and Characterization of Semiconductor Photoelectrodes with Orientation-Controlled α-Fe2O3 Thin Films, J. Phys. Chem. C. 120 (2016) 2747–2752. https://doi.org/10.1021/ACS.JPCC.5B10838.

[84] N. Danilovic, R. Subbaraman, K.C. Chang, S.H. Chang, Y.J. Kang, J. Snyder, A.P. Paulikas, D. Strmcnik, Y.T. Kim, D. Myers, V.R. Stamenkovic, N.M. Markovic, Activity-stability trends for the oxygen evolution reaction on monometallic oxides in acidic environments, J. Phys. Chem. Lett. 5 (2014) 2474–2478. https://doi.org/10.1021/jz501061n.

[85] Y.T. Kim, P.P. Lopes, S.A. Park, A.Y. Lee, J. Lim, H. Lee, S. Back, Y. Jung, N. Danilovic, V. Stamenkovic, J. Erlebacher, J. Snyder, N.M. Markovic, Balancing activity, stability and conductivity of nanoporous core-shell iridium/iridium oxide oxygen evolution catalysts, Nat. Commun. 8 (2017). https://doi.org/10.1038/s41467-017-01734-7.